Synthesis of Nb_2O_5 based solid superacid materials for catalytic combustion of chlorinated VOCs

Peng Yang[a], Shaokang Fan[a], Zhenyang Chen[a], Guofang Bao[b], Shufeng Zuo[a,*], Chenze Qi[a,*]

[a] Zhejiang Key Laboratory of Alternative Technologies for Fine Chemicals Process, Shaoxing University, Shaoxing 312000, China
[b] Shaoxing quality technology supervision and inspection institute, Shaoxing 312000, China

ARTICLE INFO

ABSTRACT

Nb_2O_5 based solid superacids (Nb_2O_5-MO_x, M = Ti, W, Zr, Si, Al and Ca, respectively) were synthesized by sol-gel method using citric acid as the cross-linking agent, and then were investigated for catalytic combustion of 1,2-dichloroethane (abbreviation: DCE), one of the typical examples for chlorinated VOCs pollutants. The research results of the structure-performance relationship show that mesopore and amorphous state structure are formed for Nb_2O_5-MO_x, and the metal elements are highly dispersed, which contribute to enhancing the metal-metal interaction and modifying the physicochemical properties of the catalysts. The order for the inherent catalytic activity is: Nb_2O_5-WO_3 > Nb_2O_5-ZrO_2 > Nb_2O_5-TiO_2 > Nb_2O_5-SiO_2 > Nb_2O_5-Al_2O_3 > Nb_2O_5 > Nb_2O_5-CaO. There exists synergistic catalytic effect: the mesopore and surface acidity facilitate the adsorption, activation and destruction of the C−Cl bond in the reactants to form HCl and byproduct C_2H_3Cl (or carbocation intermediate), and then the redox sites promote deep oxidation of the byproduct/intermediate to convert to CO_2 and H_2O. Especially, the Nb_2O_5-TiO_2 catalyst represents the highest apparent catalytic degradation activity. It also represents good thermal stability and durability for DCE destruction as well as good resistance to water vapor.

1. Introduction

VOCs contain a large kind of organic compounds with high volatility at room temperature, which are discharged from lots of industrial process [1–3]. Among them, chlorinated VOCs (or Cl-VOCs) are more toxic to the environment and human beings [3,4]. The combination of adsorption and catalytic combustion is an effective method to eliminate VOCs with low recycling value, low concentration (less than 5000 ppmv), high flow rate and complex components (such as hydrocarbons, Cl-VOCs and water), because of its higher treatment efficiency and lower reaction temperatures [5–10].

Different kinds of catalysts have been explored for destroying chlorinated VOCs: (a) supported noble metal catalysts, (b) zeolite based catalysts, (c) modified pillared clay and (d) metal oxide, perovskites or composite oxides. The application of noble metal is restricted due to their high price and easiness of deactivation by Cl poisoning [10–12]. H-type zeolite based catalysts with especial acid property and pore structure display high adsorption capacity at room temperature and noticeable catalytic activity at elevated temperature [10,13–15], but remarkable concentration of organic byproducts and CO are formed along with partial deactivation by coke formation. Modified pillared

clays with specific layer structure have been explored, but waste water is produced during the material synthesis process [16]. Perovskites with high thermal stability and facile modification are also extensively investigated, whereas their specific surface areas are smaller and higher reaction temperatures are needed [17]. In contrast, transition metal oxide and/or composite oxides (such as Cr_2O_3/Al_2O_3 [18], CeO_2-CrO_x [19], V_2O_5-NiO [20], V_2O_5-TiO_2 [21], CeO_2-TiO_2 [22], CeO_2-CuO_x [23], Fe_2O_3-ZrO_2 [24] and Co_3O_4-MnO_x-TiO_2 [25]) have drawn much more attention, and they actually display noticeable oxidative degradation activity and good resistance to coke formation and Cl-poisoning. Among them, environmentally friendly Nb_2O_5 has been studied as heterogeneous catalysts in some research field [26,27], but it has not been widely explored for Cl-VOCs oxidation. (CeO_2-CrO_x)/Nb_2O_5 with the combination of acid and oxidative property displays preferable catalytic combustion performance for 1,2-dichloroethane (abbreviation: DCE) [28]. However, to further enhance the catalytic performance, the physicochemical properties of Nb_2O_5 based catalysts should be precisely modified, and other active components (such as TiO_2, ZrO_2) can be introduced as co-catalyst or promoter to increase the catalytic selectivity to HCl and CO_2 formation as well as to promote the resistance to hot dilute hydrochloric acid.

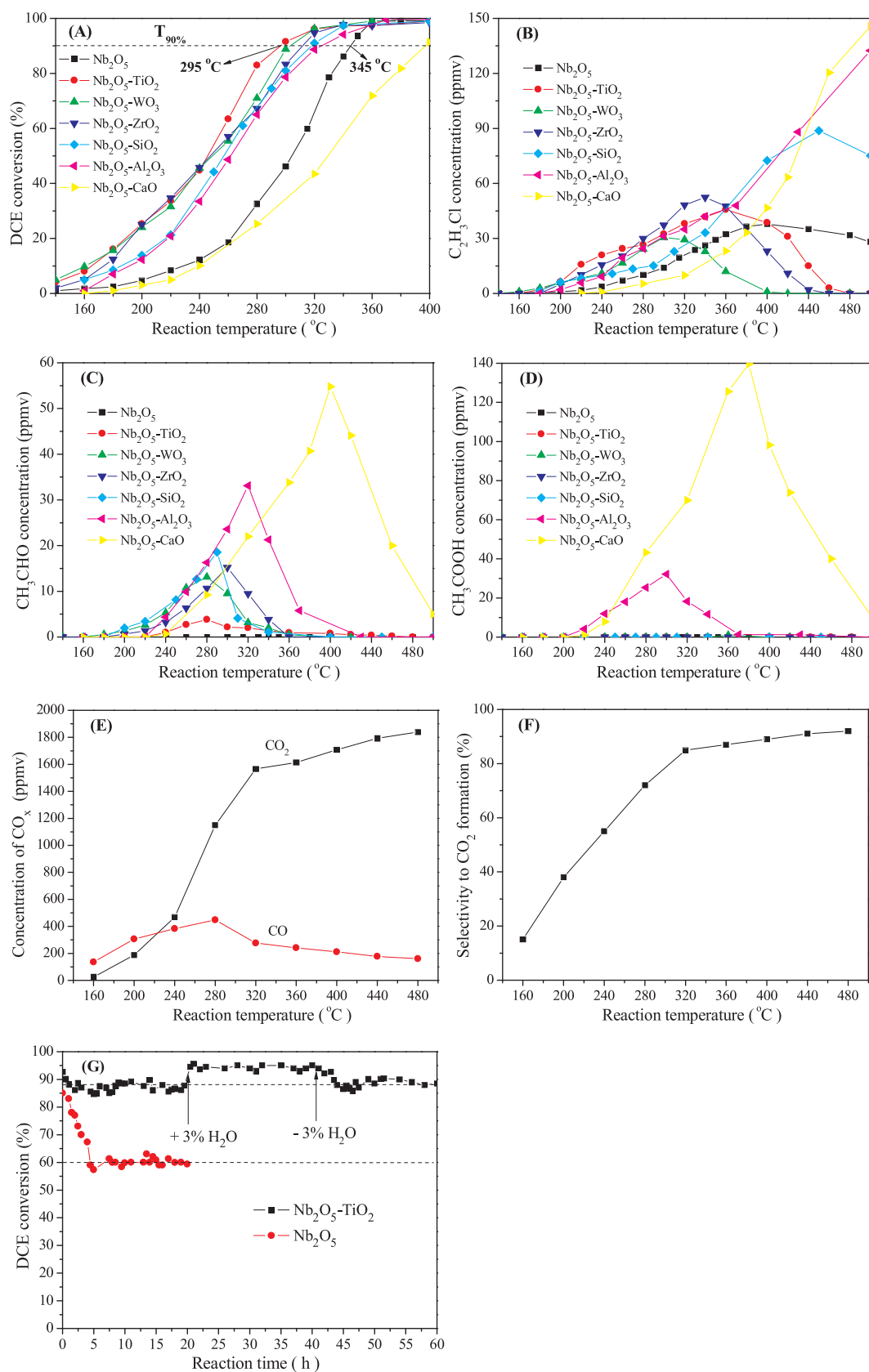**Fig. 1.** Catalytic combustion of 1,2-dichloroethane (DCE) on Nb_2O_5 based catalysts: Conversion of DCE (A); Concentration of byproduct C_2H_3Cl (B), CH_3CHO (C) and CH_3COOH (D); Evolution of CO_2 and CO for Nb_2O_5-TiO_2 (E, F); Durability test at 320 °C for Nb_2O_5 and Nb_2O_5-TiO_2 (G).

This paper aims to systematically explore the structure-function relationship for catalytic combustion of DCE on Nb_2O_5-MO_x (M = Ti, W, Zr, Si, Al and Ca, respectively). Among them, CaO is basic metal oxide, SiO_2 is neutral and Al_2O_3 is acid metal oxide, and all of them display poor redox properties. While Nb_2O_5, TiO_2, WO_3 and ZrO_2 are amphoteric metal oxide (more acid sites than basic) and they own noticeable redox properties. It concentrations on investigating the inherent catalytic nature of each transition metal oxide, the metal-metal interaction, the structure/texture and acid/redox properties of the materials, along with their synergistic catalytic effect. The influence of water vapor in the reactive gases and the durability/thermal stability of the optimized catalyst are also studied.

2. Experimental section

2.1. Material preparation

The catalysts were synthesized by typical sol-gel method, in order to mix the binary metal elements at atom level. Citric acid and ammonium oxalate niobium were premixed and dissolved in 40 mL deionized water, and then the other metal salt ($TiOSO_4$, ammonium metatungstate, $ZrO(NO_3)_3\cdot6H_2O$, $Si(OC_2H_5)_4$, $Al(NO_3)_3\cdot9H_2O$ or $Ca(NO_3)_2\cdot4H_2O$) was added under stirring condition (citric acid/(Nb + M) = 2:1, Nb/M = 2:1, molar ratio). It was heated at 80 °C until viscous gel was obtained (about 3 h). The gel was then dried in oven at 110 °C for 12 h, calcined in air at 500 °C for 2 h, and finally were pelleted and sieved to 40–60 mesh (0.3–0.45 mm) [29]. The catalysts prepared were marked as Nb_2O_5-MO_x, where M represented Ti, W, Zr, Si, Al or Ca element, respectively. Moreover, single Nb_2O_5 was also prepared by the same method.

2.2. Material characterization

The N_2 adsorption-desorption characterization was conducted at −196 °C on Micromeritics TrisStar Ⅱ 2020. The material was pretreated in high vacuum for 6 h at 200 °C. The specific surface area was calculated by the Brunauer-Emmett-Teller (BET) equation, and the micropore volume was measured by the t-plot method, while the pore size distribution and the mesopore volume were calculated by the Barrett-Joyner-Teller (BJH) method. The transmission electron microscopic (TEM) photographs were obtained on JEM-1011 operated at 200 kV, and the elemental maps were recorded by the energy dispersive spectrometer (EDS). The actual contents of the metal elements for the synthesized catalysts were measured by ICP-MS method (IRIS Intrepid II XSP). The powder X-ray diffraction (XRD) patterns were measured on D/Max-2550 pc (Cu Kα radiation, 40 kV, 40 mA). The UV-Raman spectra were collected on UV-HR Raman spectrograph, and the excitation wavelength was 514 nm of the He-Gd laser. The experiments of ammonia temperature-programmed desorption (NH_3-TPD) and hydrogen temperature-programmed reduction (H_2-TPR) were conducted by the methods described in previous references [13,30], and all the peaks in the profiles are divided by the origin software of Gaussian function fitting. The experiment of pyridine temperature-programmed desorption (pyridine-TPD) was performed similar to that of NH_3-TPD,

but the adsorption temperature was 50 °C and the flow gas was Ar (99.999%, 40 mL/min). The in-situ Fourier transform infrared spectroscopic (FTIR) measurement of pyridine adsorption-desorption experiment was conducted on CRCP-7070. Prior to pyridine adsorption at 50 °C, the samples were treated under high vacuum ($5*10^{-6}$ mbar) at 400 °C. The FTIR spectra were then recorded after evacuation at different temperatures in the range 50–400 °C.

2.3. Catalytic combustion performance evaluation

The catalytic combustion performance test of each catalyst (500 mg, 40–60 mesh) was performed in a fixed-bed quartz microreactor. The feed flow was 1000 ppmv DCE in dry air (75 mL min^{-1}), and the gas hourly space velocity (GHSV) was 9000 mL h^{-1} g_{cat}^{-1}. No mass transfer limitation is present under this reaction condition. The component and concentration of the waste gas at each given temperature were analyzed by GC, which was equipped with a FID and a TCD detector. When all organic compounds were destroyed, HCl and Cl_2 concentration were detected by chemical titration. The DCE temperature-programmed desorption/surface reaction measurement and the durability test in continuous reaction process were performed under the same reaction condition. More details are reported previously [14].

3. Results and discussion

3.1. Results of the catalytic combustion performance evaluation

Fig. 1 demonstrates the results of the catalytic combustion performances of Nb_2O_5 based materials for DCE degradation. As shown in Fig. 1(A), single-component Nb_2O_5 represents obvious catalytic combustion activity, since no obvious conversion of DCE is observed below 420 °C in the absence of catalyst. Doping different metal oxide remarkably affects the catalytic activity of Nb_2O_5 in different levels. Based on the value of $T_{90\%}$ (a certain temperature at which the DCE conversion reaches 90%), the apparent catalytic activity decreases in the sequence of Nb_2O_5-TiO_2 (295 °C) > Nb_2O_5-WO_3 (304 °C) > Nb_2O_5-ZrO_2 (311 °C) > Nb_2O_5-SiO_2 (318 °C) > Nb_2O_5-Al_2O_3 (326 °C) > Nb_2O_5 (345 °C) > Nb_2O_5-CaO (397 °C), which may be connected with the inherent nature of each transition metal oxide and its interaction with Nb_2O_5. Moreover, since the specific surface areas are quite different (shown in Table 1) and thermal effect may also exist at higher DCE conversion, the apparent reaction rates of these catalysts are calculated at low temperature (180 °C) to reflect their inherent catalytic activities. As listed in Table 1, the values decrease in the sequence of Nb_2O_5-WO_3 > Nb_2O_5-ZrO_2 > Nb_2O_5-TiO_2 > Nb_2O_5-SiO_2 > Nb_2O_5-Al_2O_3 > Nb_2O_5 > Nb_2O_5-CaO, which is consistent with the order for the apparent catalytic activity (except for Nb_2O_5-TiO_2).

As shown in Fig. 1(B)–(D), C_2H_3Cl, CH_3CHO and CH_3COOH are the organic byproducts detected in the DCE degradation process. Noticeable C_2H_3Cl is detected on Nb_2O_5, and it can not be completely destroyed at 500 °C. As to Nb_2O_5-MO_x, the order for the maximum concentration of C_2H_3Cl is: Nb_2O_5-WO_3 (31 ppmv, 300 °C) < Nb_2O_5 (38 ppmv, 360 °C) < Nb_2O_5-TiO_2 (45 ppmv, 360 °C) < Nb_2O_5-ZrO_2 (52 ppmv, 340 °C) < Nb_2O_5-SiO_2 (89 ppmv, 450 °C) < Nb_2O_5-Al_2O_3 (132

Table 1
Related data for the Nb_2O_5 based catalysts.

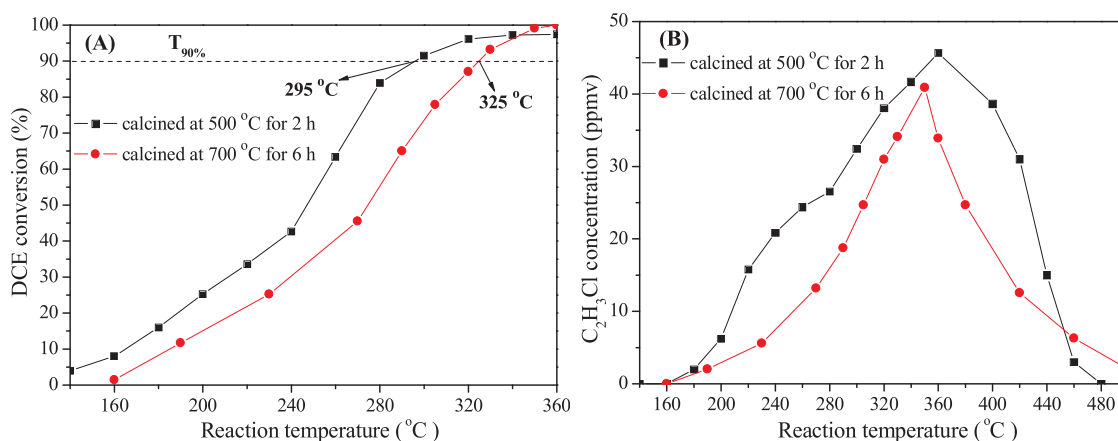| Catalyst	S_{BET}/(m²/g)	r / (10^{-11} mol_{DCE} m^{-2} s^{-1})	Micropore volume/(cm³/g)	Mesopore volume/(cm³/g)	Average pore diameter/(nm)
Nb_2O_5	33.0	2.37	0.000262	0.0741	8.9
Nb_2O_5-TiO_2	124.9	6.85	0.000177	0.0964	3.4
Nb_2O_5-WO_3	108.2	8.09	0.000431	0.173	6.7
Nb_2O_5-ZrO_2	99.0	7.00	0.00290	0.120	5.3
Nb_2O_5-SiO_2	138.6	3.44	0.00607	0.153	5.1
Nb_2O_5-Al_2O_3	150.0	2.61	0.000250	0.125	3.5
Nb_2O_5-CaO	28.0	0.199	0.000320	0.118	17.3

Fig. 2. Degradation of DCE on Nb$_2$O$_5$-TiO$_2$ calcined in air at different temperatures: (A) DCE conversion; (B) Byproduct C$_2$H$_3$Cl concentration.
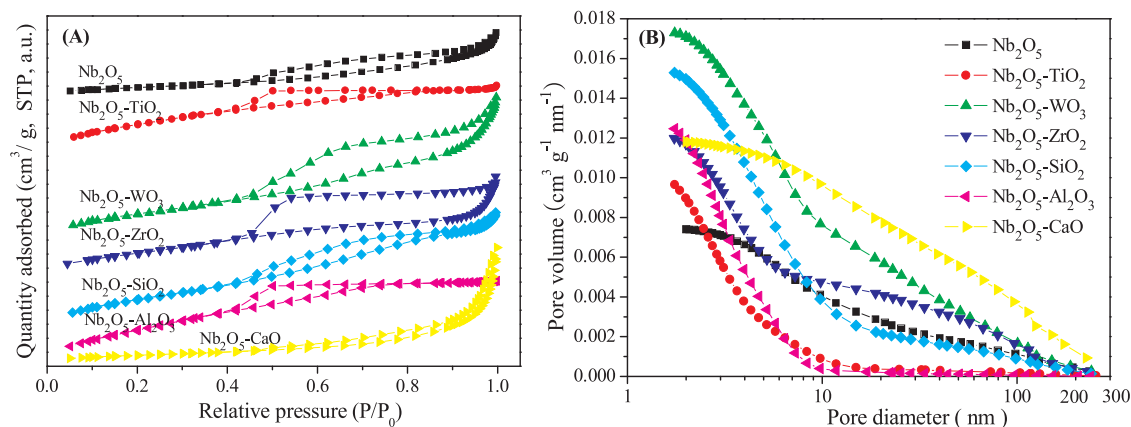

Fig. 3. The adsorption-desorption isotherms (A) and pore size distribution (B) of Nb$_2$O$_5$ based catalysts.

ppmv, 500 °C) < Nb$_2$O$_5$-CaO (146 ppmv, 500 °C). As to the concentration of byproduct CH$_3$CHO, the order is similar, in the order of Nb$_2$O$_5$ < Nb$_2$O$_5$-TiO$_2$ < Nb$_2$O$_5$-WO$_3$ < Nb$_2$O$_5$-ZrO$_2$ < Nb$_2$O$_5$-SiO$_2$ < Nb$_2$O$_5$-Al$_2$O$_3$ < Nb$_2$O$_5$-CaO. And large concentration of CH$_3$COOH is only detected on Nb$_2$O$_5$-Al$_2$O$_3$ and Nb$_2$O$_5$-CaO, indicating their poor oxidizing ability. In all, the above results display that these catalysts represent different catalytic activity and selectivity, and the structure-function relationship will be investigated and discussed below.

Moreover, for deep oxidation of chlorinated VOCs, the final products are HCl/Cl$_2$, CO$_2$/CO and H$_2$O. The data of S$_{HCl}$ (selectivity to the formation of HCl, the desired product) and S$_{CO2}$ (selectivity to the formation of CO$_2$) for Nb$_2$O$_5$-TiO$_2$ is 95% and 85%, respectively (measured at 320 °C), which deserves more attention and may be further improved by doping third metal element and/or optimizing reaction condition. Furthermore, at this temperature, the carbon and chlorine balance is 97.2% and 98.5%, respectively, implying that slight C and Cl species are deposited on the catalyst in the DCE degradation process.

To further study the performance of the Nb$_2$O$_5$-TiO$_2$ catalyst, the evolution of the reactant, any possible byproducts and the final products in the reaction system are tracked by MS in the dynamic catalytic process, and the results are shown in Fig. S1 in Supplementary material. As shown in Fig. S1, a remarkable DCE desorption peak appears at 93 °C, and its appearance is accompanied with the emergence of C$_2$H$_3$Cl and HCl, implying that the desorption is coupled with degradation [30]. Deep catalytic oxidation of the DCE and C$_2$H$_3$Cl occurs above 200 °C, coupled with their sharp decrease and the emergence of CO$_x$, and it can be finished at 350 °C. This catalyst displays higher selectivity to the formation of HCl and CO$_2$, which are the preferable final products. These results are consistent with the results of the catalytic performance

test at the steady-state condition mentioned above.

The durability of the Nb$_2$O$_5$ and Nb$_2$O$_5$-TiO$_2$ catalysts are evaluated at 320 °C and the results are displayed in Fig. 1(G). As shown in Fig. 1(G), DCE conversion over Nb$_2$O$_5$ drops sharply in the first 4.5 h, and then it maintains at about 60% in the rest time. The partial deactivation may be related to the coke/Cl species deposition on the catalyst surface [19]. As to Nb$_2$O$_5$-TiO$_2$, however, only slight deactivation is detected in the first 1 h, and DCE conversion is stabilized at about 88%. Interestingly, if 3% water steam is introduced in the reaction system, the catalytic activity of Nb$_2$O$_5$-TiO$_2$ increases, which can be related to the n-type semiconductor form of Nb$_2$O$_5$ and TiO$_2$ as well as the quick removal of surface coke/Cl species away from the catalyst. This situation is quite different from the (CeO$_2$-CrO$_x$)/Nb$_2$O$_5$ and the (CeO$_2$-CrO$_x$)/HZSM-5 catalyst system, over which the catalytic activities decrease because of the competitive adsorption effect of water [13,28]. Moreover, if water is removed away, the activity recovered, indicating its good resistance to hot dilute hydrochloric acid.

The thermal stability of the Nb$_2$O$_5$-TiO$_2$ catalyst is further evaluated and the result is displayed in Fig. 2. As shown in Fig. 2, DCE conversion drops slightly after the catalyst is calcined at 700 °C for 6 h, and the T$_{90\%}$ value increases from 295 to 325 °C, while the corresponding concentration of byproduct C$_2$H$_3$Cl decreases slightly. As presented in Fig. S2 in Supplementary material, the crystal of TiNb$_2$O$_7$ (reference code: 00-039-1407) is formed for the aged catalyst, which is different from the fresh catalyst (amorphous state and/or high dispersion). Moreover, the specific surface area decreases from 124.9 to 23.8 m^2/g, while the mesopore volume is almost unchanged (0.0970 cm^3/g), and the average pore diameter increases from 3.4 to 16.8 nm. Encouragingly, the catalytic combustion performance does not decrease sharply after severe aging, and the TiNb$_2$O$_7$ mixed oxide generated
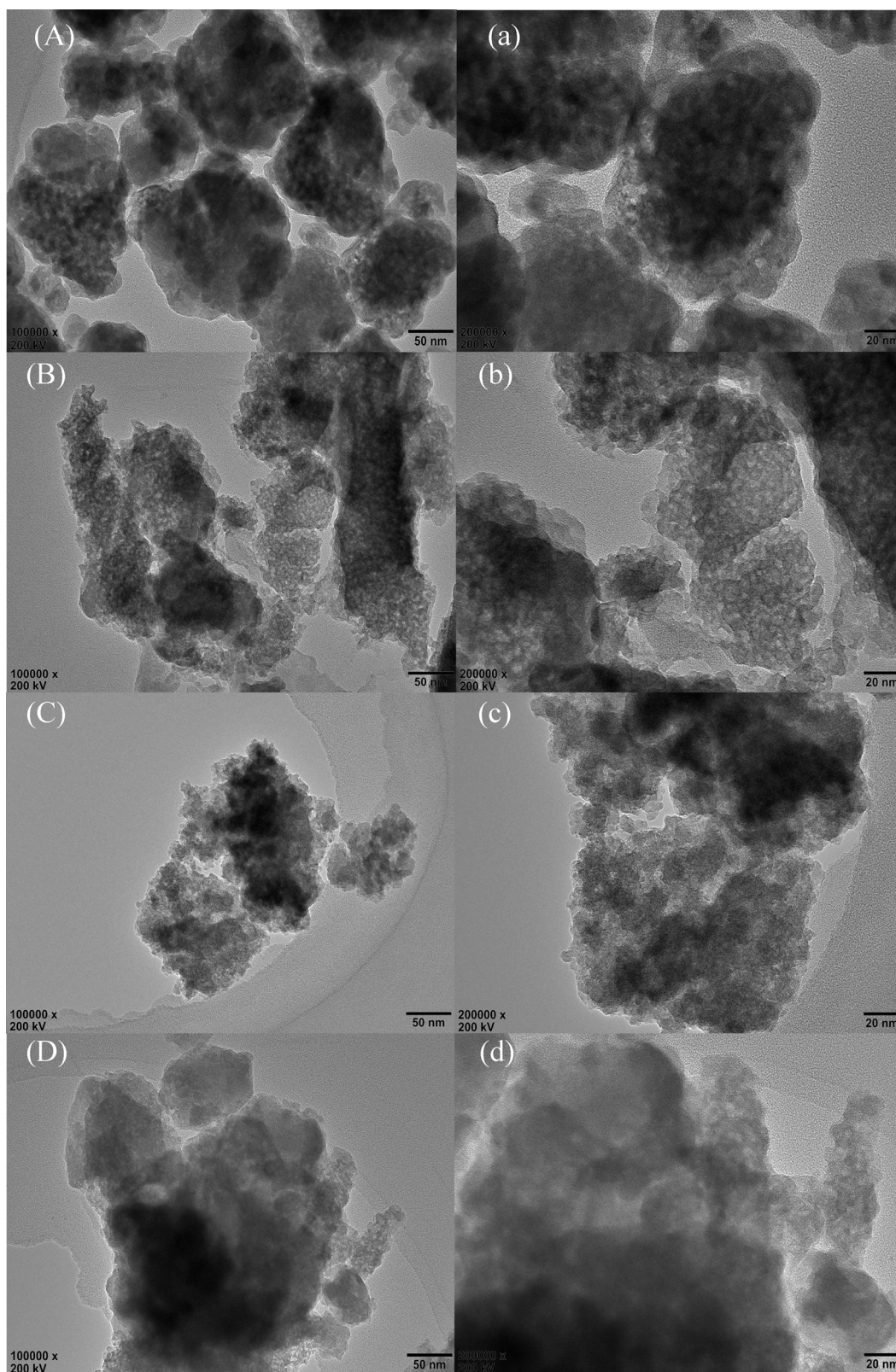
Fig. 4. The TEM pictures of Nb_2O_5 based catalysts: (A, a) Nb_2O_5, (B, b) Nb_2O_5-TiO_2, (C, c) Nb_2O_5-WO_3, (D, d) Nb_2O_5-ZrO_2, (E, e) Nb_2O_5-SiO_2, (F, f) Nb_2O_5-Al_2O_3 and (G, g) Nb_2O_5-CaO. The EDS spectra of Nb_2O_5-TiO_2 are also shown (a'–e').

would present better behaviour per meter square than the amorphous state and/or high dispersion of the fresh catalyst. These results show that the Nb_2O_5-TiO_2 catalyst can suffer heat shock in a short period, which is also important for industrial consideration.

3.2. Results of catalyst characterization

3.2.1. N_2 adsorption/desorption characterization

In general, the texture/structure properties of the catalysts are
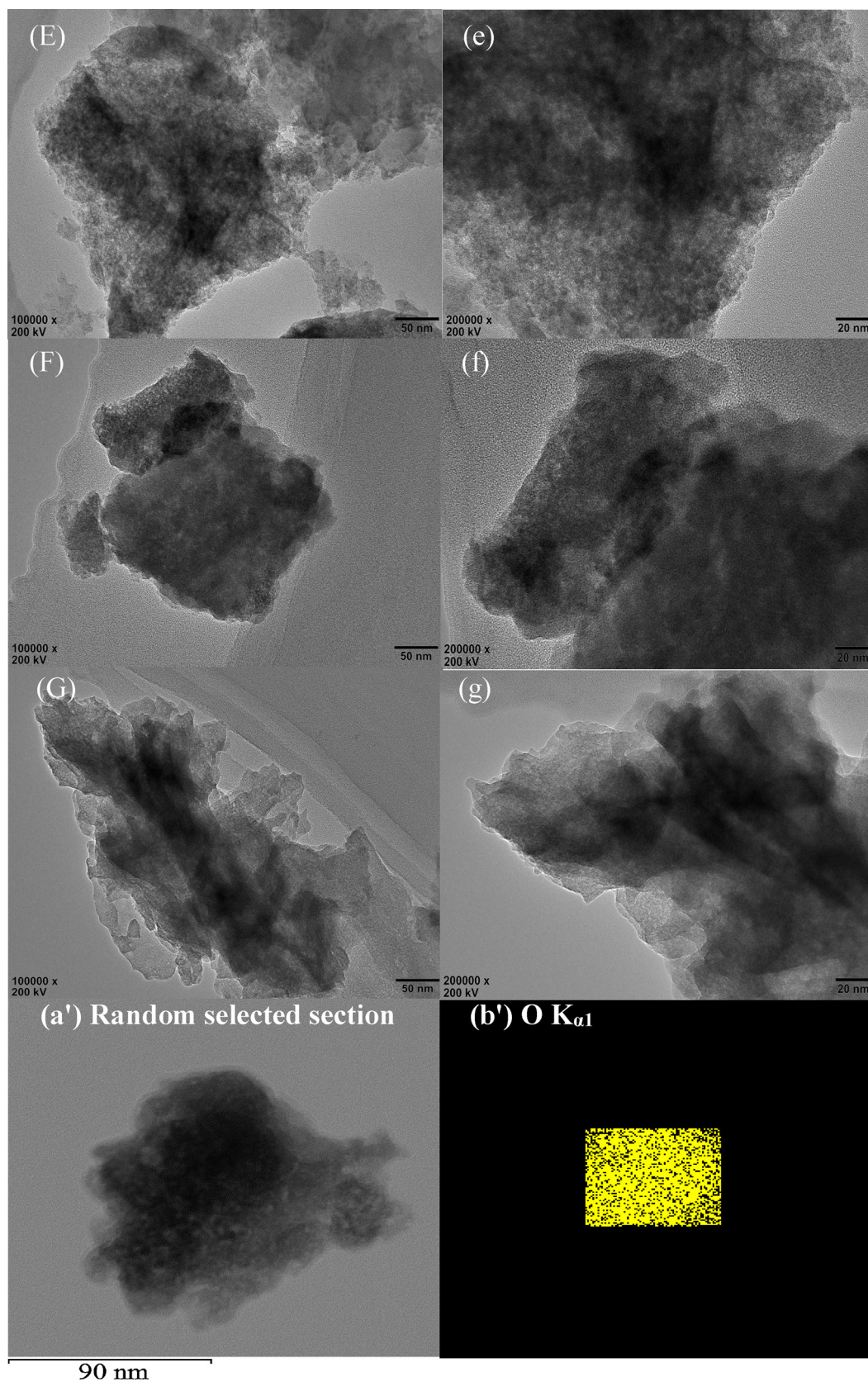
Fig. 4. (*continued*)

important for the surface catalytic reaction, especially under the reaction condition of high gas space velocity and large gas flow volume. And it is noteworthy that the kinetic diameter of the DCE molecule is about 0.54 nm. Based on practical experience, the pore channel of the catalysts should be more than five times larger than the DCE molecule size to overcome the mass transfer limit. Thus, for this catalytic reaction, the mesopores of the catalytic materials are more important than the micropores. The pore structure properties of the catalysts are shown

Fig. 4. (*continued*)

in Fig. 3 and the related data are listed in Table 1.

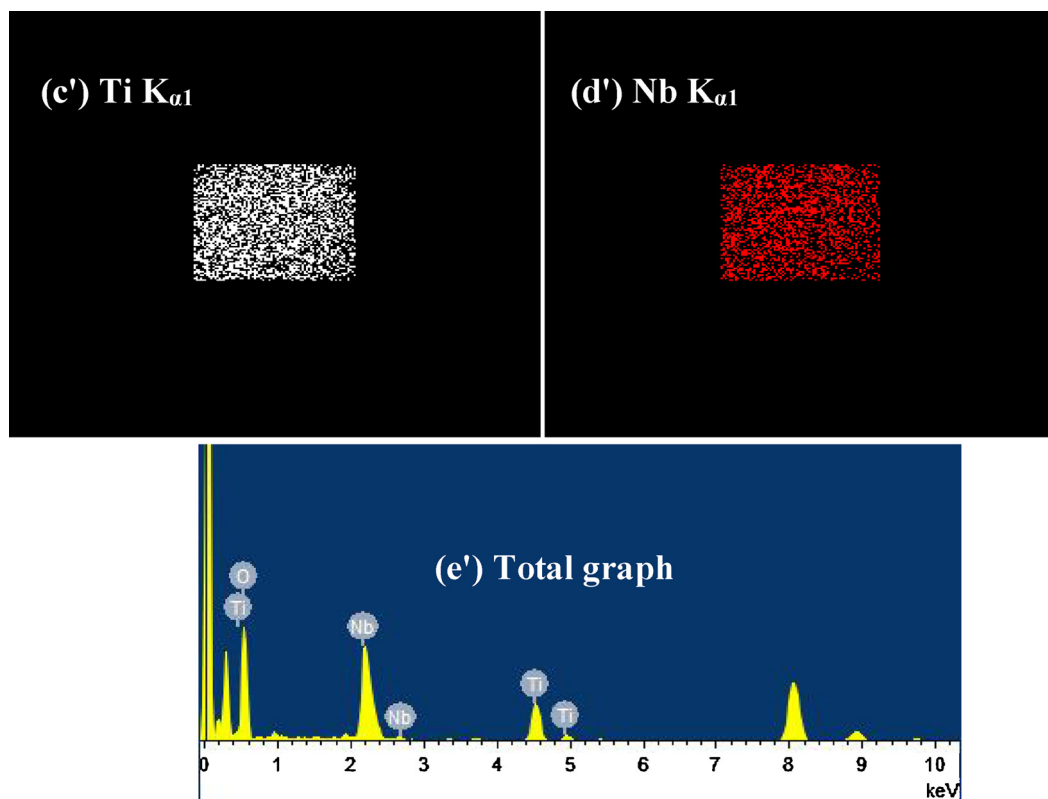As presented in Fig. 3(A), the adsorption-desorption isotherms of Nb_2O_5-TiO_2 and Nb_2O_5-Al_2O_3 present hysteresis type H2, while other catalysts belong to type III and the hysteresis loops belong to the H3 type [31]. These results indicate that they exhibit micropore/mesopore composite structure. As presented in Fig. 3(B), most of the materials display wide pore size distribution, except for Nb_2O_5-TiO_2 and Nb_2O_5-Al_2O_3 (smaller than 10 nm), and the average pore diameter decreases in the order of Nb_2O_5-CaO > Nb_2O_5 > Nb_2O_5-WO_3 > Nb_2O_5-ZrO_2, Nb_2O_5-SiO_2 > Nb_2O_5-Al_2O_3, Nb_2O_5-TiO_2. The micropores and mesopores are mainly from the internal channel of the materials, while the macropores are mainly generated from the buildup of the catalyst particles. As listed in Table 1, similar to Nb_2O_5, Nb_2O_5-MO_x shows much larger mesopore volume than micropore volume. The values of the mesopore volume decrease in the order of Nb_2O_5-WO_3 > Nb_2O_5-SiO_2 > Nb_2O_5-ZrO_2, Nb_2O_5-Al_2O_3, Nb_2O_5-CaO > Nb_2O_5-TiO_2 > Nb_2O_5, and the values of the specific surface area decrease in the order of Nb_2O_5-Al_2O_3 > Nb_2O_5-SiO_2 > Nb_2O_5-TiO_2 > Nb_2O_5-WO_3 > Nb_2O_5-ZrO_2 > Nb_2O_5 > Nb_2O_5-CaO. However, these orders are not directly related to that of the $T_{90\%}$ value for DCE elimination, indicating that the texture property of this catalyst system is only one of the factors affecting the catalytic performance, which is similar to the CeO_2-CrO_x and the (CeO_2-CrO_x)/zeolite catalyst system [13,14,19].

3.2.2. TEM characterization

Fig. 4 presents the TEM images of the Nb_2O_5 and Nb_2O_5-MO_x catalysts, and the elemental distribution mapping for Nb_2O_5-TiO_2 is also given. As shown in Fig. 4(A, a), Nb_2O_5 is blocky-shaped particle, and its diameter is not uniform. For Nb_2O_5-MO_x displayed in Fig. 4(B, b)–(G, g), their morphology are different from each other. The diameters of all these catalysts are also not uniform, and the dissociation of Nb_2O_5 and MO_x can not be detected by visual inspection. Particularly, as shown in Fig. 4(B, b) and (a')–(e'), Nb_2O_5-TiO_2 represents smaller particle size, and the elemental distribution of Nb, Ti and O is uniform (molar ratio of Nb/Ti is 2.04, three random sections have been investigated and the

results are almost the same, therefore only one section is shown here), which suggests that the Nb and Ti element can be highly dispersed into each other by the sol-gel preparation method. Moreover, the actual contents of the metal elements in the bulk Nb_2O_5-TiO_2 catalyst are also measured and the molar ratio of Nb/Ti is 2.02 (53.8 wt.% for Nb, 13.7 wt.% for Ti), very close to the theoretical values, since no loss of metal elements occurs in the catalyst synthesis process (water in the mixed solution was evaporated, and then the obtained gel was dried and calcined).

3.2.3. XRD and Raman characterization

Fig. 5 represents the XRD and the Raman patterns of the Nb_2O_5 and Nb_2O_5-MO_x catalysts. As shown in Fig. 5(A), crystals are mainly observed for single Nb_2O_5 (reference code: 00-007-0061, Hexagonal crystal system), and slight amorphous states also exist due to the non-level baseline. As to all the Nb_2O_5-MO_x catalysts, however, two broad peaks in the range of 19–39 ° and 43–67 ° are observed, and the characteristic diffraction peaks of Nb_2O_5 and MO_x can not be clearly detected (slight $Nb_2W_3O_{14}$ is detected for Nb_2O_5-WO_3, reference code: 00-025-1357, Tetragonal crystal system), which could be due to the high dispersion of Nb_2O_5 and MO_x and/or their amorphous states. It is worth noting that the ionic radius decreases in order of Ca^{2+} (1.00 Å) > Zr^{4+} (0.720 Å) > Nb^{5+} (0.640 Å) > Ti^{4+} (0.605 Å) > W^{6+} (0.600 Å) > Al^{3+} (0.535 Å) > Si^{4+} (0.400 Å). Thus, other Nb−O−M mixed oxides (such as $TiNb_2O_7$, $ZrNb_2O_7$ and $AlNbO_4$) may also be formed at higher calcination temperatures or under certain conditions by partially substituting Nb^{5+} by M^{n+} in the Nb_2O_5 lattice, while Nb−O−Ca or Nb−O−Si mixed oxides can not be formed. However, in this context it is difficult to identify an unambiguous identification of these crystals, due to the significant line broadening of the XRD patterns. These results indicate that amorphous states are mainly formed for Nb_2O_5-MO_x, which can be associated with the existence of strong Nb−O−M bonds to inhibit the movement of metal ions required to initiate the phase formation [32].

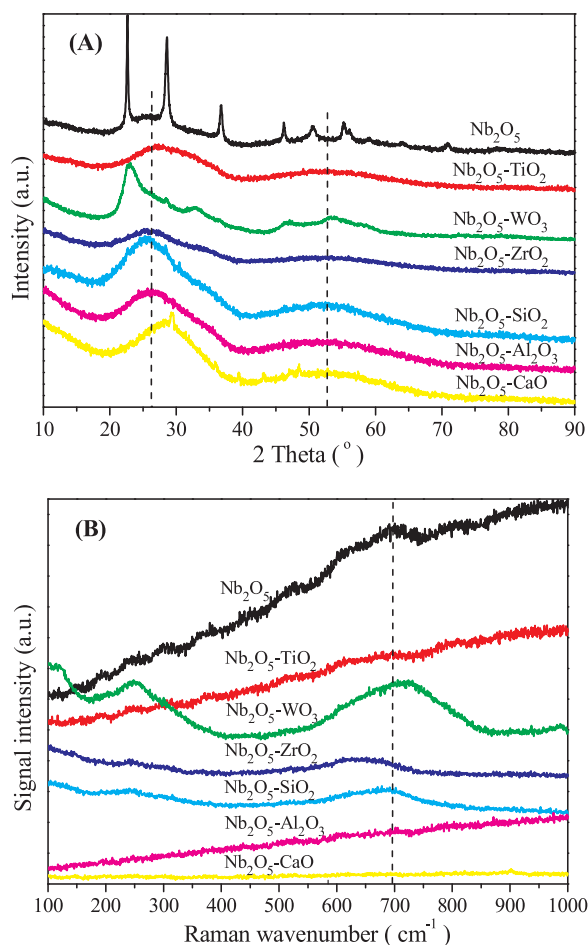Be different from the XRD technique, the Raman spectra are

Fig. 5. The (A) XRD and (B) Raman patterns of Nb_2O_5 based catalysts.

sensitive to the crystalline symmetry [28,33] and thus can be a supplement for structure research. As shown in Fig. 5(B), as to Nb_2O_5, its spectrum is dominated by a broad band at 696 cm^{-1}, which is typical for NbO_x and is ascribed to the vibration of Nb−O−Nb bridge from the slightly distorted octahedral NbO_6 connected with sharing corners. The band around 890 cm^{-1} can be assigned to the symmetric stretching mode of surface Nb=O species, present in the highly distorted octahedral NbO_6. Raman bands between 150 and 300 cm^{-1} are due to the bending modes of Nb−O−Nb linkages [34]. The absence of Raman-active modes corresponding to NbO_x reveals that Nb_2O_5 is amorphous in the materials. Moreover, the Raman patterns of Nb_2O_5-MO_x are much weaker than single Nb_2O_5, and the position and shape of the characteristic peaks are different, generated from the strong metal-metal interaction between Nb_2O_5 and MO_x [35–37]. Particularly, as to Nb_2O_5-WO_3, the characteristic peaks are broader and more obvious, while the typical Raman bands for WO_3 phase are not detected [38], which may be related to the stronger interaction between Nb_2O_5 and WO_3 leading to the formation of slight $Nb_2W_3O_{14}$, in line with the XRD characterization results.

3.2.4. NH$_3$-TPD characterization

As to the Cl-VOC molecule, the polarity of C−Cl chemical bond is larger than others, due to the electronegativity of the Cl atom. Thus, the C−Cl bond is easier to be adsorbed, activated and dissociated by the surface acidity of the catalysts (in the form of HCl on the Brønsted acid sites and/or metal chloride on the Lewis acid sites), which are the first steps for catalytic combustion of various Cl-VOCs. The NH$_3$-TPD technique is adopted to measure the surface acid property of the catalysts, and the results are exhibited in Fig. 6.
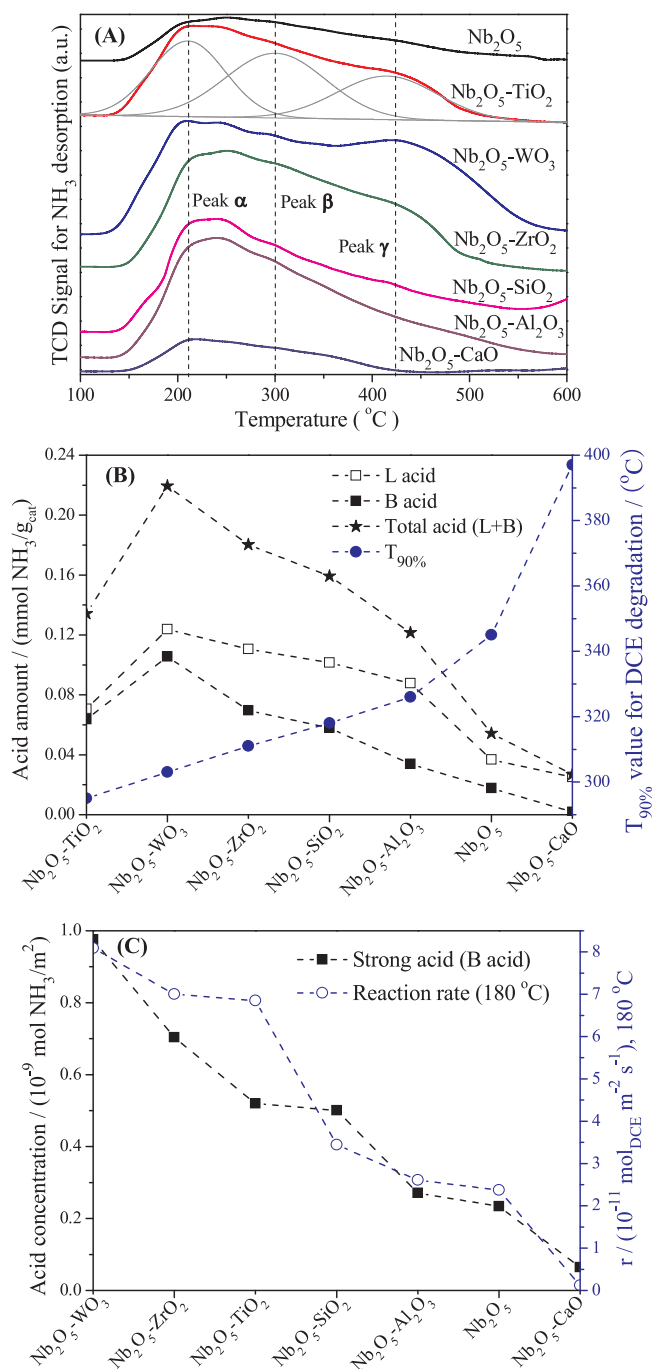

Fig. 6. The NH$_3$-TPD curves of the Nb_2O_5 and Nb_2O_5-MO_x catalysts.

As presented in Fig. 6(A), three broad peaks (peak α, β and γ) are detected for all the catalysts, which are concentrated in 210, 300 and 420 °C, attributed to the desorption of NH$_3$ adsorbed on the weak/moderate acid (M^{n+}-O, the Lewis acid sites) and the strong acid (−OH, the Brønsted acid sites), respectively [14,28,37–41]. The coexistence of L and B acid sites is also confirmed by the pyridine-TPD and in-situ FTIR techniques [42], as shown in Fig. S3 in the Supplementary material of this work. Moreover, the surface of Nb_2O_5 is known to be covered with acidic sites comparable to the strength of 70% sulphuric acid ($H_0 = -5.6$) [39], and it is noticeable that the strong acid strength of these catalysts is comparable to the H-USY zeolite (displayed in Fig. S4 in Supplementary material), which is a typical solid superacid. As shown in Fig. 6(B), except for Nb_2O_5-TiO_2, the orders for the amount of the Brønsted acid, Lewis acid and total acid centers (as well as the ratio of
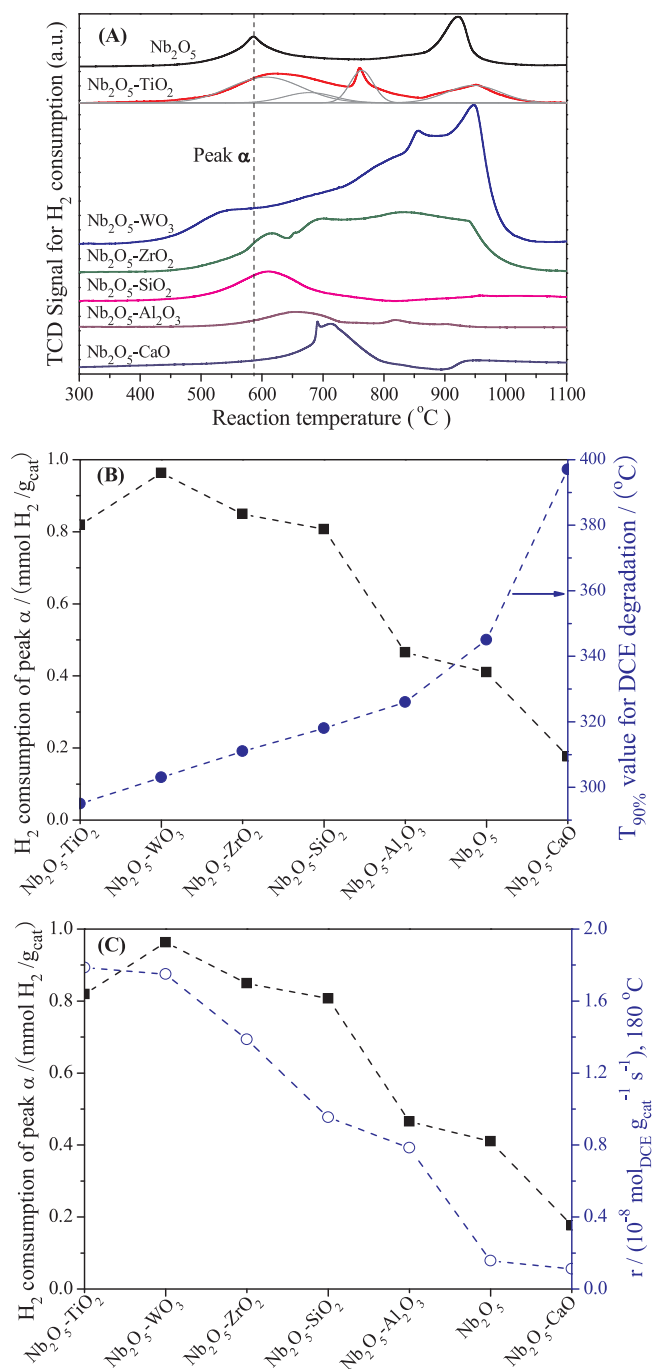
Fig. 7. The H$_2$-TPR curves of the Nb$_2$O$_5$ and Nb$_2$O$_5$-MO$_x$ catalysts.

Brønsted/Lewis acid amount) are in the same: Nb$_2$O$_5$-WO$_3$ > Nb$_2$O$_5$-ZrO$_2$ > Nb$_2$O$_5$-SiO$_2$ > Nb$_2$O$_5$-Al$_2$O$_3$ > Nb$_2$O$_5$ > Nb$_2$O$_5$-CaO, which are negatively correlated with the order for the T$_{90\%}$ value of DCE conversion and the maximum concentration of byproduct C$_2$H$_3$Cl. These results indicate that in the catalytic combustion process, improving the acid properties of the catalytic materials can promote the degradation of the DCE reactant and suppress the formation of the byproduct C$_2$H$_3$Cl. As to Nb$_2$O$_5$-TiO$_2$, though its acid property is less than Nb$_2$O$_5$-WO$_3$ and Nb$_2$O$_5$-ZrO$_2$, it displays the highest apparent catalytic activity. As shown in Fig. 6(C), its apparent reaction rate is also less than Nb$_2$O$_5$-WO$_3$ and Nb$_2$O$_5$-ZrO$_2$, indicating than the larger specific surface area of Nb$_2$O$_5$-TiO$_2$ can also be helpful for DCE elimination. And the order for the strong acid sites concentration of the catalysts is same as the apparent reaction rate. Moreover, as shown in Fig. 6(C), the concentration

of the strong acid sites have a larger magnitude than the apparent reaction rate, which implies that partial acid sites take no part in the catalytic reaction. It may be related to that the NH$_3$ is smaller than the DCE, therefore, the DCE molecule cannot reach the acid sites in the smaller pores of the catalysts.

3.2.5. H$_2$-TPR characterization

Generally, improving the redox property of a certain catalyst is beneficial for deep oxidation of the VOCs. The H$_2$-TPR technique is employed to characterize the redox properties of the Nb$_2$O$_5$ and Nb$_2$O$_5$-MO$_x$ catalysts, and the results are displayed in Fig. 7.

As presented in Fig. 7(A), as to single Nb$_2$O$_5$, two obvious reduction peaks are detected at about 585 (peak α) and 922 °C (peak β), respectively, which are ascribed to the reduction of surface/subsurface oxygen and the reduction of partial bulk oxygen, respectively [28]. As to Nb$_2$O$_5$-MO$_x$, apart from the peak α, H$_2$ consumption peaks at higher temperatures are also detected, due to the reduction of high-valence metal oxides and/or the partial bulk oxygen [28,43]. The peak position and shape of peak α are also different, resulted from the strong interaction of Nb$_2$O$_5$ and MO$_x$. Particularly, compared to Nb$_2$O$_5$, peak α appears at lower temperature for Nb$_2$O$_5$-WO$_3$ due to the formation of Nb−W−O mixed oxide. Whereas it appears at higher temperature for Nb$_2$O$_5$-Al$_2$O$_3$, and it is much weaker for Nb$_2$O$_5$-CaO, suggesting that Nb$_2$O$_5$-Al$_2$O$_3$ and Nb$_2$O$_5$-CaO are more difficult to be reduced, and thus their oxidizing ability is also much weaker. As shown in Fig. 7(B) and (C), except for Nb$_2$O$_5$-TiO$_2$, the order for the H$_2$ consumption of peak α is: Nb$_2$O$_5$-WO$_3$ > Nb$_2$O$_5$-ZrO$_2$ > Nb$_2$O$_5$-SiO$_2$ > Nb$_2$O$_5$-Al$_2$O$_3$ > Nb$_2$O$_5$ > Nb$_2$O$_5$-CaO, which is negatively correlated with the order for the T$_{90\%}$ values, the apparent reaction rate (180 °C) and the maximum concentration of the byproduct C$_2$H$_3$Cl, indicating that improving the redox property can enhance deep oxidation of the reactant and the possible byproduct formed in the oxidation process. And this result is similar to the result of NH$_3$-TPD characterization. Particularly, though the H$_2$ consumption of peak α for the Nb$_2$O$_5$-TiO$_2$ catalyst is not the largest, its larger specific surface area may also be helpful for the DCE elimination.

In conclusion, it can be seen from the above results that compared to Nb$_2$O$_5$, both the physical and chemical property of Nb$_2$O$_5$-MO$_x$ can be modified at the same time by doping different metal oxides. In the process for catalytic combustion of DCE, the mesopore structure and surface acidity of Nb$_2$O$_5$-MO$_x$ promote the reactant DCE occurring adsorption at room temperature, then activation and dehydrochlorination at elevated temperature to convert to HCl and byproduct C$_2$H$_3$Cl (part of C$_2$H$_3$Cl interacts with the surface hydroxy to form $^+$CH$_2$−CH$_2$−Cl carbocation), while the oxidative property of the Nb$_2$O$_5$-MO$_x$ contributes to the complete deep oxidation to CO$_2$ and H$_2$O, and finally the reduced reactive sites can be reoxidized by gaseous oxygen molecule to fulfill the catalytic recycle. Therefore, synergistic catalytic effect is generated from the coexistence of mesopore structure, acid and redox centers in the Nb$_2$O$_5$-MO$_x$ catalyst system. It is consistent with our previous research result for DCE elimination on the (Ce,Cr)$_x$O$_2$/zeolite catalyst system [13,14,30], but much less byproducts are detected on Nb$_2$O$_5$-TiO$_2$ reported in the recent work. Similar situations have also been observed in the dual-functional Pd/Cr$_2$O$_3$-ZrO$_2$ catalyst for dichloromethane oxidation [44], the VO$_x$/TiO$_2$-CeO$_2$ catalyst for chlorobenzene oxidation [45] and the SnO$_2$-Al$_2$O$_3$ nano-rod for toluene total oxidation [46].

Particularly, the Nb$_2$O$_5$-WO$_3$ catalyst displays the best inherent catalytic activity, and its texture property (such as the specific surface area) should be further improved. The Nb$_2$O$_5$-TiO$_2$ catalyst displays the best apparent catalytic activity, and it also represents good durability and good resistance to thermal shock as well as dilute hydrochloric acid corrosion. Both of them are solid superacid with good redox property and have the advantages of low price and environmental safety, which deserve more research attention for application consideration.

4. Conclusions

Nb$_2$O$_5$ based solid superacid materials (Nb$_2$O$_5$-MO$_x$, M = Ti, W, Zr, Si, Al and Ca, respectively) were synthesized by sol-gel method using citric acid, and used for catalytic combustion of low concentration 1,2-dichloroethane (abbreviation: DCE), as one of the typical examples for chlorinated VOCs. These catalysts were characterized by several physicochemical techniques, and the results show that Nb$_2$O$_5$-MO$_x$ are mainly mesoporous structures and the metal ions are highly dispersed into each other, which contributes to improving the metal-metal interaction. Compared to single Nb$_2$O$_5$, the physicochemical properties of Nb$_2$O$_5$-MO$_x$ are significantly modified by doping MO$_x$. The increase of either acid or redox property promotes the catalytic combustion performances of Nb$_2$O$_5$-MO$_x$ for DCE combustion, and the order for the apparent catalytic activity is as follows: Nb$_2$O$_5$-TiO$_2$ > Nb$_2$O$_5$-WO$_3$ > Nb$_2$O$_5$-ZrO$_2$ > Nb$_2$O$_5$-SiO$_2$ > Nb$_2$O$_5$-Al$_2$O$_3$ > Nb$_2$O$_5$ > Nb$_2$O$_5$-CaO. In the catalytic degradation process of chlorinated VOCs, the acid property facilitates the destruction of the C-Cl bond in the reactants to form HCl, and the redox property promotes the deep catalytic oxidation of the organic intermediates/byproducts converted to CO$_2$ and H$_2$O. Especially, Nb$_2$O$_5$-TiO$_2$ exhibits the best apparent catalytic activity, and it also represents good thermal stability, good durability for DCE destruction as well as good resistance to water vapor during the constant reaction test, which implies that this catalyst system deserves more research attention and may be potential for future industrial application.

Acknowledgments

Appendix A. Supplementary data

Supplementary material related to this article can be found, in the online version, at doi:https://doi.org/10.1016/j.apcatb.2018.07.061.

References

[1] X.Y. Zhang, B. Gao, A.E. Creamer, C.C. Cao, Y.C. Li, Adsorption of VOCs onto engineered carbon materials: a review, J. Hazard. Mater. 338 (2017) 102–123.

[2] A. Śrębowata, R. Baran, G. Słowik, D. Lisovytskiy, S. Dzwigaj, Influence of the postsynthesis preparation procedure on catalytic behaviour of Ag-loaded BEA zeolites in the hydrodechlorination of 1,2-dichloroethane into value added products, Appl. Catal. B-Environ. 199 (2016) 514–522.

[3] A. Martucci, E. Rodeghero, L. Pasti, V. Bosi, G. Cruciani, Adsorption of 1,2-dichloroethane on ZSM-5 and desorption dynamics by in situ synchrotron powder X-ray diffraction, Microporous Mesoporous Mater. 215 (2015) 175–182.

[4] J. González-Prior, R. López-Fonseca, J.I. Gutiérrez-Ortiz, B. de Rivas, Catalytic removal of chlorinated compounds over ordered mesoporous cobalt oxides synthesised by hard-templating, Appl. Catal. B-Environ. 222 (2018) 9–17.

[5] C.C. Du, S.Y. Lu, Q.L. Wang, A.G. Buekens, M.J. Ni, D.P. Debecker, A review on catalytic oxidation of chloroaromatics from flue gas, Chem. Eng. J. 334 (2018) 519–544.

[6] C.H. Dai, Y.Y. Zhou, H. Peng, S.J. Huang, P.F. Qin, J.C. Zhang, Y. Yang, L. Luo, X.S. Zhang, Current progress in remediation of chlorinated volatile organic compounds: a review, J. Ind. Eng. Chem. 62 (2018) 106–119.

[7] A.N. Zagoruiko, V.V. Mokrinskii, S.A. Veniaminov, A.S. Noskov, On the performance stability of the MnO$_x$/Al$_2$O$_3$ catalyst for VOC incineration under forced adsorption-catalytic cycling conditions, J. Environ. Chem. Eng. 5 (2017) 5850–5856.

[8] M.S. Kamal, S.A. Razzak, M.M. Hossain, Catalytic oxidation of volatile organic compounds (VOCs)–a review, Atmos. Environ. 140 (2016) 117–134.

[9] Z.X. Zhang, Z. Jiang, W.F. Shangguan, Low-temperature catalysis for VOCs removal in technology and application: a state-of-the-art review, Catal. Today 264 (2016) 270–278.

[10] A. Aranzabal, B. Pereda-Ayo, M.P. González-Marcos, J.A. González-Marcos, R. López-Fonseca, J.R. González-Velasco, State of the art in catalytic oxidation of chlorinated volatile organic compounds, Chem. Pap. 68 (2014) 1169–1186.

[11] Z. Boukh, J. González-Prior, B. de Rivas, J.R. González-Velasco, R. López-Fonseca, J.I. Gutiérrez-Ortiz, Pd supported catalyst for gas-phase 1,2-dichloroethane abatement: efficiency and high selectivity towards oxygenated products, J. Ind. Eng. Chem. 57 (2018) 77–88.

[12] Z.E. Assal, S. Ojala, S. Pitkäaho, L. Pirault-Roy, B. Darif, J.D. Comparot, M. Bensitel, R.L. Keiski, R. Brahmi, Comparative study on the support properties in the total oxidation of dichloromethane over Pt catalysts, Chem. Eng. J. 313 (2017) 1010–1022.

[13] P. Yang, S.F. Zuo, R.X. Zhou, Synergistic catalytic effect of (Ce,Cr)$_x$O$_2$ and HZSM-5 for elimination of chlorinated organic pollutants, Chem. Eng. J. 323 (2017) 160–170.

[14] P. Yang, Z.N. Shi, F. Tao, S.S. Yang, R.X. Zhou, Synergistic performance between oxidizability and acidity/texture properties for 1,2-dichloroethane oxidation over (Ce,Cr)$_x$O$_2$/zeolite catalysts, Chem. Eng. Sci. 134 (2015) 340–347.

[15] R. López-Fonseca, J.I. Gutiérrez-Ortiz, J.L. Ayastui, M.A. Gutiérrez-Ortiz, J.R. González-Velasco, Gas-phase catalytic combustion of chlorinated VOC binary mixtures, Appl. Catal. B-Environ. 45 (2003) 13–21.

[16] S.F. Zuo, P. Yang, X.Q. Wang, Efficient and environmentally friendly synthesis of AlFe-PILC-supported MnCe catalysts for benzene combustion, ACS Omega 2 (2017) 5179–5186.

[17] S. Maghsoodi, J. Towfighi, A. Khodadadi, Y. Mortazavi, The effects of excess manganese in nano-size lanthanum manganite perovskite on enhancement of tri-chloroethylene oxidation activity, Chem. Eng. J. 215–216 (2013) 827–837.

[18] R. Ma, P.J. Hu, L.Y. Jin, Y.J. Wang, J.Q. Lu, M.F. Luo, Characterization of CrO$_x$/Al$_2$O$_3$ catalysts for dichloromethane oxidation, Catal. Today 175 (2011) 598–602.

[19] P. Yang, Z.N. Shi, S.S. Yang, R.X. Zhou, High catalytic performances of CeO$_2$–CrO$_x$ catalysts for chlorinated VOCs elimination, Chem. Eng. Sci. 126 (2015) 361–369.

[20] H.F. Huang, X.X. Zhang, K. Dou, X.J. Jiang, H.F. Lu, Influence of oxide support to the Ni-V catalysts in the catalytic oxidation of dichloromethane, J. Environ. Sci. 36 (2016) 3273–3279.

[21] J. Wang, X. Wang, X.L. Liu, J.L. Zeng, Y.Y. Guo, T.Y. Zhu, Kinetics and mechanism study on catalytic oxidation of chlorobenzene over V$_2$O$_5$/TiO$_2$ catalysts, J. Mol. Catal. A-Chem. 402 (2015) 1–9.

[22] S. Cao, H.Q. Wang, F.X. Yu, M.P. Shi, S. Chen, X.L. Weng, Y. Liu, Z.B. Wu, Catalyst performance and mechanism of catalytic combustion of dichloromethane (CH$_2$Cl$_2$) over Ce doped TiO$_2$, J. Colloid Interface Sci. 463 (2016) 233–241.

[23] C. He, Y.K. Yu, C.W. Chen, L. Yue, N.L. Qiao, Q. Shen, J.S. Chen, Z.P. Hao, Facile preparation of 3D ordered mesoporous CuO$_x$–CeO$_2$ with notably enhanced efficiency for the low temperature oxidation of heteroatom-containing volatile organic compounds, RSC Adv. 3 (2013) 19639–19656.

[24] Z. Zhang, H.Q. Xia, Q.G. Dai, X.Y. Wang, Dichloromethane oxidation over Fe$_x$Zr$_{1-x}$ oxide catalysts, Appl. Catal. A-Gen. 557 (2018) 108–118.

[25] J. Mei, Z. Qu, S.J. Zhao, X.F. Hu, H.M. Xu, N.Q. Yan, Promoting effect of Mn and Ti on the structure and performance of Co$_3$O$_4$ catalysts for oxidation of dibromoethane, J. Colloid Interface Sci. 505 (2017) 870–883.

[26] M. Ziolek, I. Sobczak, The role of niobium component in heterogeneous catalysts, Catal. Today 285 (2017) 211–225.

[27] L.C.A. Oliveira, M.F. Portilho, A.C. Silva, H.A. Taroco, P.P. Souza, Modified niobia as a bifunctional catalyst for simultaneous dehydration and oxidation of glycerol, Appl. Catal. B-Environ. 117–118 (2012) 29–35.

[28] P. Yang, S.F. Zuo, Z.N. Shi, F. Tao, R.X. Zhou, Elimination of 1,2-dichloroethane over (Ce,Cr)$_x$O$_2$/MO$_y$ catalysts (M = Ti, V, Nb, Mo, W and La), Appl. Catal. B-Environ. 191 (2016) 53–61.

[29] P. Yang, Z.H. Meng, S.S. Yang, Z.N. Shi, R.X. Zhou, Highly active behaviors of CeO$_2$–CrO$_x$ mixed oxide catalysts in deep oxidation of 1,2-dichloroethane, J. Mol. Catal. A-Chem. 393 (2014) 75–83.

[30] P. Yang, X.M. Xue, Z.H. Meng, R.X. Zhou, Enhanced catalytic activity and stability of Ce doping on Cr supported HZSM-5 catalysts for deep oxidation of chlorinated volatile organic compounds, Chem. Eng. J. 234 (2013) 203–210.

[31] K.S.W. Sing, D.H. Everett, R.A.W. Haul, L. Moscou, R.A. Pierotti, J. Rouquérol, T. Siemieniewska, Reporting physisorption data for gas/solid systems with special reference to the determination of surface area and porosity, Pure Appl. Chem. 57 (1985) 603–619.

[32] N.P. Ferraz, F.C.F. Marcos, A.E. Nogueira, A.S. Martins, M.R.V. Lanza, E.M. Assaf, Y.J.O. Asencios, Hexagonal-Nb$_2$O$_5$/Anatase-TiO$_2$ mixtures and their applications in the removal of Methylene blue dye under various conditions, Mater. Chem. Phys. 198 (2017) 331–340.

[33] P. Yang, S.S. Yang, Z.N. Shi, Z.H. Meng, R.X. Zhou, Deep oxidation of chlorinated VOCs over CeO$_2$-based transition metal mixed oxide catalysts, Appl. Catal. B-Environ. 162 (2015) 227–235.

[34] D. Stošić, S. Bennici, V. Pavlović, V. Rakić, A. Auroux, Tuning the acidity of niobia: characterization and catalytic activity of Nb$_2$O$_5$-MeO$_2$ (me = Ti, Zr, Ce) mesoporous mixed oxides, Mater. Chem. Phys. 146 (2014) 337–345.

[35] T. Kim, A. Burrows, C.J. Kiely, I.E. Wachs, Molecular/electronic structure–surface acidity relationships of model-supported tungsten oxide catalysts, J. Catal. 246 (2007) 370–381.

[36] M. Anilkumar, W.F. Hoelderich, New non-zeolitic Nb-based catalysts for the gas-phase Beckmann rearrangement of cyclohexanone oxime to caprolactam, J. Catal. 293 (2012) 76–84.

[37] M. Massa, A. Andersson, E. Finocchio, G. Busca, F. Lenrick, L.R. Wallenberg, Performance of ZrO$_2$-supported Nb- and W-oxide in the gas-phase dehydration of glycerol to acrolein, J. Catal. 297 (2013) 93–109.

[38] J. Guo, S.H. Zhu, Y.L. Cen, Z.F. Qin, J.G. Wang, W.N. Fan, Ordered mesoporous Nb–W oxides for the conversion of glucose to fructose, mannose and 5-hydroxymethylfurfural, Appl. Catal. B-Environ. 200 (2017) 611–619.

[39] Y. Zhao, C. Eley, J.P. Hu, J.S. Foord, L. Ye, H.Y. He, S.C.E. Tsang, Shape-dependent acidity and photocatalytic activity of Nb$_2$O$_5$ nanocrystals with an active TT (001) surface, Angew. Chem. Int. Ed. 51 (2012) 3846–3849.

[40] A. Aronne, M. Turco, G. Bagnasco, G. Ramis, E. Santacesaria, M.D. Serio, E. Marenna, M. Bevilacqua, C. Cammarano, E. Fanelli, Gel derived niobium–silicon mixed oxides: characterization and catalytic activity for cyclooctene epoxidation, Appl. Catal. A-Gen. 347 (2008) 179–185.

[41] K. Yamashita, M. Hirano, K. Okumura, M. Niwa, Activity and acidity of Nb_2O_5-MoO_3 and Nb_2O_5-WO_3 in the friedel-crafts alkylation, Catal. Today 118 (2006) 385–391.

[42] S. Gillot, G. Tricot, H. Vezin, J.P. Dacquin, C. Dujardin, P. Granger, Development of stable and efficient $CeVO_4$ systems for the selective reduction of NO_x by ammonia: structure-activity relationship, Appl. Catal. B-Environ. 218 (2017) 338–348.

[43] K.V.R. Chary, K.R. Reddy, C.P. Kumar, D. Naresh, V.V. Rao, G. Mestl, Characterization and reactivity of molybdenum oxide catalysts supported on

[44] Nb_2O_5–TiO_2, J. Mol. Catal. A-Chem. 223 (2004) 363–369.

[44] L.Y. Jin, R.H. Ma, J.J. Lin, L. Meng, Y.J. Wang, M.F. Luo, Bifunctional Pd/Cr_2O_3-ZrO_2 catalyst for the oxidation of volatile organic compounds, Ind. Eng. Chem. Res. 50 (2011) 10878–10882.

[45] C. Gannoun, R. Delaigle, D.P. Debecker, P. Eloy, A. Ghorbel, E.M. Gaigneaux, Effect of support on V_2O_5 catalytic activity in chlorobenzene oxidation, Appl. Catal. A-Gen. 447–448 (2012) 1–6.

[46] Y. Liu, Y. Guo, Y.Q. Liu, X.L. Xu, H.G. Peng, X.Z. Fang, X. Wang, SnO_2 nano-rods promoted by in, Cr and Al cations for toluene total oxidation: the impact of oxygen property and surface acidity on the catalytic activity, Appl. Surf. Sci. 420 (2017) 186–195.